



Effect of substituent position on aggregation-induced emission, customized self-assembly, and amine detection of donor-acceptor isomers: Implication for meat spoilage monitoring

Jingdan Hou^a, Jiaorui Du^b, Yue Hou^a, Peijun Shi^a, Yang Liu^c, Yuai Duan^{a,*}, Tianyu Han^{a,*}

^a Department of Chemistry, Capital Normal University, Beijing 100048, China

^b School of Chemistry, Beijing Institute of Technology, Beijing 100081, China

^c Beijing Key Laboratory of Radiation Advanced Materials, Beijing Research Center for Radiation Application, Beijing 100015, China

ARTICLE INFO

Article history:

Received 7 May 2018

Received in revised form 20 June 2018

Accepted 7 July 2018

Available online 09 July 2018

Keywords:

Aggregation-induced emission

Self-assembly

Position effect

Amine sensor

Meat spoilage

ABSTRACT

We synthesized a class of positional isomers by attaching electron donor and acceptor units in different sites of a conjugated core. These isomers exhibit both aggregation-induced emission (AIE) and intramolecular charge transfer (ICT) effects, which are proved by adequate spectroscopic analysis. Their structure-property relationships were systematically studied. We found that relocation of the D/A units would have remarkable impact on the intermolecular dipole-dipole interaction, further controlling the shape and color of the self-assembled architectures. With D/A units shifting to different sites, four types of the structures appear sequentially, including quadrate microsheets, microrods, nanofilaments and nanowires. Furthermore, the A unit (benzoic acid moiety) of the AIE isomers is easy to adsorb amines, leading to changes in both emission wavelength and intensity. Then a portable sensor is prepared on solid support based on the self-assembled architecture of HMBA-4, which has been proved to be the most sensitive to amines. It affords fast spectral responses as well as a low detection limit of 186 Pa (vapour pressure). The sensing mechanism was revealed by density functional theory (DFT) calculation, which indicates that the spectral responses stem from the weakened ICT effect. The sensor is able to detect amine vapours generated by meat, and thus succeeds in detecting the spoiled pork samples, offering high potential for meat spoilage monitoring in real-world applications.

© 2018 Elsevier B.V. All rights reserved.

1. Introduction

As huge amount of meat products is stored and shipped all over the world every year, food safety has attracted increasing attention because it is closely related to human health and economic issue. Relevant food monitoring techniques have been developed, which are mostly based on mass spectrometry [1,2], electrochemical method [3,4], and nuclear magnetic resonance (NMR) spectrometer [5]. By contrast, optical sensors or techniques are easier to use, owing to their fast response, on-line visual inspection and low-cost measurement [6–8]. In search of optical sensors, aggregation-induced emission (AIE) molecular systems have emerged as a quickly growing research hotspot [9–14]. The beauty of AIE stems from the fact that the molecules are designed to be highly twisted to ensure high emission efficiency at solid state, in which the intermolecular π - π stacking have been avoided to suppress the formation of excimer/excimer [15]. Thus the AIE-based sensors are compatible with various solid supports such as thin films, nano-carriers, and polymer substrates [16–18]. Given that some specific amines would be

generated in degradation of proteins, they could be regarded as an indicator for food spoilage. Inspired by this fact, some examples of AIE-based sensors for food spoilage detection have been reported recently [19,20]. And the mechanism of the above-mentioned AIE sensors mainly involves a specific chemical reaction between AIE sensor and amines. However, change in chemical structure may suffer from insufficient conversion or prolonged reaction time, and these disadvantages could be even more serious in solid-gas reactions [20].

AIE materials capable of emission switching by changing molecular packing mode are believed to be an alternative way to fabricate fluorescent sensors including those for meat spoilage detection. This design philosophy focuses on the changes in aggregation structure instead of that in molecular structure, and relies heavily on the self-assembly techniques. Nano/micro-sized sensor systems built via self-assemblies have emerged as a highly growing field, and a large number of studies have revealed that the self-assemblies will inherit the sensing performances or optical properties of the isolated molecules, and benefit a great deal from their high-ordered molecular packing [21–23]. Just as the application of fluorescent sensors based on molecular self-assembled structure took several years longer to optimize than simply on molecular structure, so too has the application of AIE sensor lagged

* Corresponding author.

E-mail addresses: duanya@cnu.edu.cn (Y. Duan), phanw@163.com (T. Han).

behind on self-assembly [24–26]. An elegant way to create the building blocks is incorporating the electron donor (D) and acceptor (A) substituents to AIE cores, which may yield highly polarized luminogens with high solid-state emission [27–29]. D-A type AIE systems would enable the intramolecular charge transfer (ICT) phenomena [30–32], and further provide strong dipole-dipole interactions for self-assembly [33]. Another advantage of D-A pairs stems from their high degree of freedom, which means the species, numbers and spatial position of the D-A units are highly controllable, making the molecular designing extremely diversified. This open-choice principle undoubtedly facilitates the systematic study on the relationships between supramolecular structures and optical properties, by which the working mechanisms of the functional subjects would be revealed. This would pave ways for the development of tailor-made optical sensors and smart materials for a given application, including AIE-based ones [34–36].

In this work, we present a new AIE molecular system based on positional isomers. The relationship between the D-A position and the corresponding self-assembly structure was investigated. These AIE isomers exhibit obvious solvatochromic effect in solution and emit long-wavelength fluorescence ranging from yellow to orange in the solid state. The AIE molecules show fluorescent responses to amine gas, and hence we aimed to find an applicable AIE compound showing the best performance to serve as an indicator for meat spoilage.

2. Experimental Section

2.1. Instruments and Methods

Reagents and chemicals were purchased from Tokyo Chemical Industry (TCI) and Alfa Aesar and used as received without further purification. ^1H NMR and ^{13}C NMR spectra were measured on a Varian VNMRs 600 MHz spectrometer using tetramethylsilane as an internal reference. The molecular weights were determined on an Agilent 7500Ce inductively coupled plasma source mass spectrometer (ICP-mass). Emission spectra were recorded on a HITACHI F-7000 FL spectrophotometer. UV-vis spectra were measured on a SHIMADZU UV-2550 spectrophotometer. The fluorescence quantum yields (ϕ_{F}) were determined using a calibrated integrating sphere on a HORIBA FluoroMax-4 (relative error: 0.017). The ground-state geometries were optimized using density functional theory (DFT) with the B3LYP hybrid functional at the basis set level of 6-31G*. The calculations were performed with Gaussian 05 package. Fluorescence images were taken under an Olympus CKX41 phase contrast microscope (excitation wavelength: 365 nm). Powder X-ray diffraction (PXRD) patterns were collected with monochromatized Cu-K α 1 ($\lambda = 1.54178 \text{ \AA}$) incident radiation by a Shimadzu XRD-6000 instrument. The images of the morphology were captured using a Hitachi SU-8010 scanning electron microscope (SEM). The thickness of the sensing film was measured by a Smart-Sensor Coating/Filming thickness gauge.

2.2. Synthesis and Structural Characterization

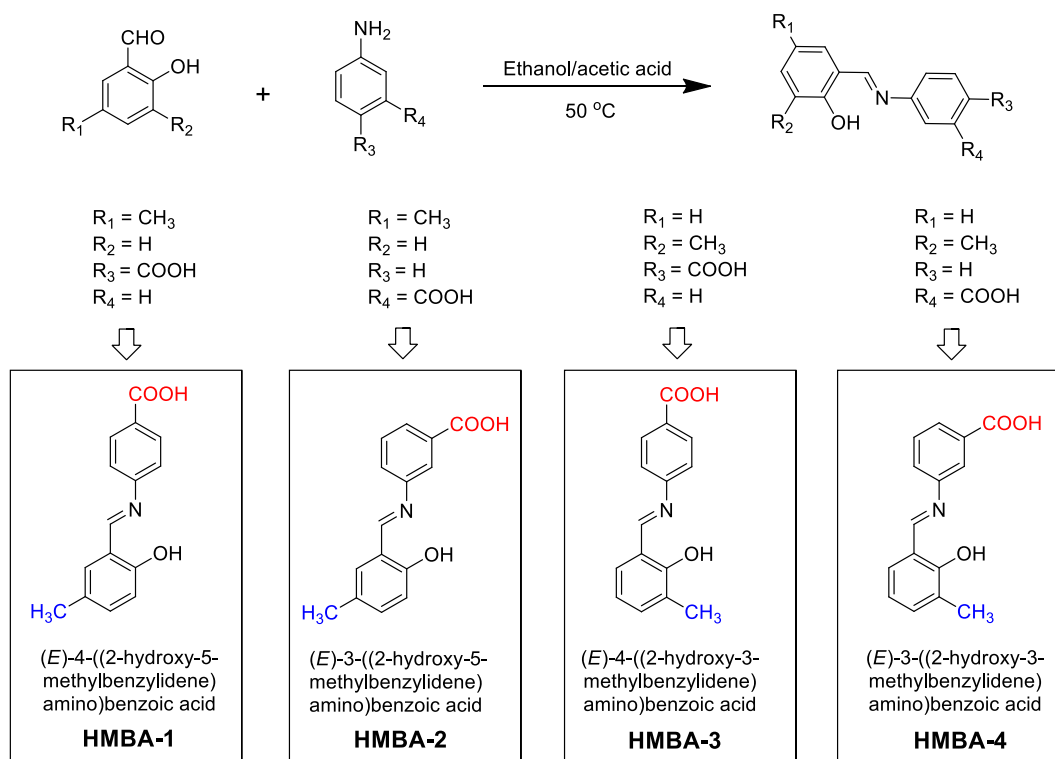
The synthetic route to the AIE isomers including (E)-4-((2-hydroxy-5-methylbenzylidene)amino)benzoic acid (HMBA-1), (E)-3-((2-hydroxy-5-methylbenzylidene)amino)benzoic acid (HMBA-2), (E)-4-((2-hydroxy-3-methylbenzylidene)amino)benzoic acid (HMBA-3) and (E)-3-((2-hydroxy-3-methylbenzylidene)amino)benzoic acid (HMBA-4) are illustrated in Scheme 1. Detailed synthetic procedure of HMBA-1 is described as follows. To a solution of 2-hydroxy-5-methylbenzaldehyde (1.00 g, 7.34 mmol, 1 equiv) in anhydrous ethanol (150 mL) was added 4-aminobenzoic acid (1.01 g, 7.34 mmol, 1 equiv), 0.1 mL acetic acid was added to the reaction mixture before it was heated to 50 °C. The reaction mixture was then stirred for 2 h, yielding HMBA-1 as yellow crystalline powder. The resulting products were collected by vacuum filtration using ethanol to rinse. No further purification was needed. Yield: 62%. The synthesis of HMBA-2, HMBA-3 and

HMBA-4 were prepared according to the procedure of HMBA-1 with some modifications, including an extended reaction time (15 h) and an elevated reaction temperature (60 °C). Yields of HMBA-2, HMBA-3 and HMBA-4 were 45%, 60% and 50%, respectively. The structures of the four compounds were well characterized by ^1H NMR and ^{13}C NMR spectroscopy with satisfactory analysis results (Figs. S1–S8). Below are data obtained from their structural characterization. ^1H NMR of HMBA-1 (600 MHz, DMSO d_6), δ (ppm): 12.92 (s, 1H), 12.38 (s, 1H), 8.90 (s, 1H), 8.00–7.97 (m, 2H), 7.47 (d, 1H), 7.45–7.43 (m, 2H), 7.25–7.23 (dd, 1H), 6.87–6.86 (d, 1H), 2.26 (s, 3H). ^{13}C NMR of HMBA-1 (151 MHz, DMSO d_6), δ (ppm): 167.30, 165.00, 158.58, 152.78, 135.04, 132.67, 131.16, 129.12, 128.30, 121.90, 119.44, 116.98, 20.36. ICP-Mass of HMBA-1: calcd 256.10 [(M + H) $^+$], found 255.90]. ^1H NMR of HMBA-2 (600 MHz, DMSO d_6), δ (ppm): 13.12 (s, 1H), 12.51 (s, 1H), 8.94 (s, 1H), 7.87 (t, 1H), 7.85–7.84 (dt, 1H), 7.63–7.61 (dq, 1H), 7.57–7.55 (t, 1H), 7.48–7.47 (d, 1H), 7.23–7.21 (dd, 1H), 6.86–6.85 (d, 1H), 2.25 (s, 3H). ^{13}C NMR of HMBA-2 (151 MHz, DMSO d_6), δ (ppm): 167.36, 164.64, 158.52, 149.11, 134.75, 132.78, 132.57, 130.22, 128.19, 127.87, 126.39, 122.16, 119.43, 116.91, 20.38. ICP-Mass of HMBA-2: calcd 256.10 [(M + H) $^+$], found 256.20]. ^1H NMR of HMBA-3 (600 MHz, DMSO d_6), δ (ppm): 13.29 (s, 1H), 12.93 (br s, 1H), 8.98 (s, 1H), 8.01–7.99 (m, 2H), 7.51–7.47 (m, 3H), 7.33–7.32 (d, 1H), 6.90–6.88 (t, 1H), 2.20 (s, 3H). ^{13}C NMR of HMBA-3 (151 MHz, DMSO d_6), δ (ppm): 167.28, 166.16, 159.28, 151.96, 135.05, 131.42, 131.16, 129.32, 125.63, 121.97, 119.21, 118.64, 15.62. ICP-Mass of HMBA-3: calcd 256.10 [(M + H) $^+$], found 256.20]. ^1H NMR of HMBA-4 (600 MHz, DMSO d_6), δ (ppm): 13.37 (s, 1H), 13.14 (s, 1H), 9.01 (s, 1H), 7.92 (t, 1H), 7.87–7.85 (dt, 1H), 7.67–7.66 (dq, 1H), 7.59–7.56 (t, 1H), 7.50–7.49 (dd, 1H), 7.32–7.30 (d, 1H), 6.90–6.87 (t, 1H), 2.21 (s, 3H). ^{13}C NMR of HMBA-4 (151 MHz, DMSO d_6), δ (ppm): 167.34, 165.64, 159.16, 148.47, 134.80, 132.62, 131.35, 130.24, 128.04, 126.56, 125.54, 122.12, 119.15, 118.71, 109.99, 15.65. ICP-Mass of HMBA-4: calcd 256.10 [(M + H) $^+$], found 255.90]. (Abbreviations: br = broad, s = singlet, d = doublet, t = triplet, q = quartet).

3. Results and Discussion

3.1. Aggregation-induced Emission

Luminogens are commonly used in solid state, such as thin films, nano-aggregates, crystals and self-assembled architectures. Thus it would be necessary to increase the emission efficiency at solid state. It has been reported frequently that AIE luminogens are able to overcome the emission quenching effect by twisting their molecular conformation to break π - π stacking. Such mechanism, well known as “restriction of intramolecular motion (RIM)” is supported by plenty of evidence, led to an explosion of new AIE systems [15,18]. The first step of this study was to merge the electron donor-acceptor (D-A) pairs to form the desired luminogens HMBA-1, 2, 3 and 4 (HMBAs), by using a facile Schiff base reaction. Obviously the propeller-shaped molecular design contributing to AIE mechanism facilitates the creation of the HMBAs, in which benzylideneaniline moiety serves as conjugated chromophore, C—C and C—N single bonds offer the possibility of both intramolecular rotation in solution and conformation twisting in aggregation. Additionally, the incorporation of D-A units could fine tune the energy of ground and excited state, by which the energy gap is narrowed to generate photo-excited emission with longer wavelength. The photoluminescence (PL) spectra of the HMBAs in the solid state together with their photos under UV irradiation are shown in Fig. 1. For HMBA-1, the emission peak is located at around 545 nm, which is assigned to the intramolecular charge transfer (ICT) emission. When the carboxylic group was changed from para-position to meta-position, the corresponding compound HMBA-2 exhibits a bathochromic-shift and peaked at 552 nm in the emission spectrum. Similarly, if methyl group was shifted to another meta-position, i.e., ortho-position of phenolic hydroxyl, the emission wavelength



Scheme 1. Synthetic route to HBMA-1, -2, -3 and -4. D and A units are highlighted in blue and red color, respectively. (For interpretation of the references to color in this figure legend, the reader is referred to the web version of this article).

undergoes an even bigger red-shift (from 545 nm to 574 nm) as seen in HMBA-3 (Fig. 1). When attaching both D and A units to the meta-position (HMBA-4), the emission wavelength changes to 556 nm. The results demonstrate that the ICT emission can be well controlled by the position of D-A units.

The first way to test whether they are AIE-active is to confirm their quantum efficiency in both solution and solid state. The absolute Φ_F values of these molecules in solution and the solid state were obtained using the calibrated integrating sphere, and then summarized in Table 1. All quantum yields of the THF solution are low and fall in the range of 0.22% to 1.41%. In contrast, they are remarkably increased at

the solid state. When comparing the solution of HMBA-1, 2, 3 and 4 to their solid powder, there is an approximate 38, 25, 10 and 2.34-fold increase in Φ_F , respectively. Presumably the lack of emission in solution is due to the vibrational and torsional relaxation, while the significant increase of Φ_F in solid state suggests the nonradiative relaxations are inhibited by the motionless rigid matrix.

The emission behavior of the four compounds was investigated through typical AIE experiments, which is done by dissolving each luminogen in pure THF or DMSO and then adding hexane or water as a poor solvent. The PL spectrum was collected at every increment of poor solvent. Typically, HMBA-1 was almost non-emissive in THF solution as shown in Fig. 2A. Increase of the hexane fraction (f_h) from 10% to 90% exerts no change in PL spectra, because HMBA-1 is still solvated. When f_h reaches 99%, there is a significant boost of the PL intensity at 535 nm, affording approximately a 688-fold enhancement relative to that in pure THF solution. HMBA-2 and HMBA-3 shows a similar spectral change as displayed in Fig. 2B and C. They exhibit 87 and 227-fold enhancement in emission intensity, respectively. In comparison, the AIE effect of HMBA-4 is much weaker: there is still weak emission in DMSO solution and the enhancement in emission intensity is

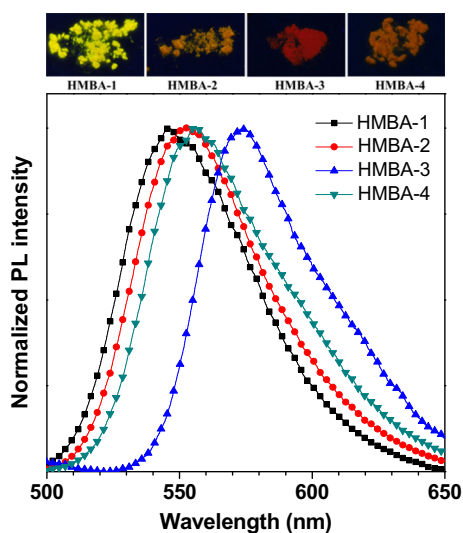


Fig. 1. PL spectra of the solid powders of HBMA-1, -2, -3 and -4. Excitation wavelength: 350 nm (HMBA-1), 340 nm (HMBA-2), 375 nm (HMBA-3 and HMBA-4). Photographs of the solid powders were taken under UV irradiation from a hand-held UV lamp.

Table 1

Photophysical data of the HBMA-1, -2, -3 and -4. Abbreviation: $\lambda_{ab,DMSO}$ = maximum absorption wavelength in DMSO solution (10 μM), $\lambda_{em,P}$ = maximum emission wavelength of the solid powders, $\lambda_{em,aggr}$ = maximum emission wavelength of the aggregates formed in poor solvents, $\lambda_{em,F}$ = maximum emission wavelength of the self-assembly films, $\Phi_{F,S}$ = absolute quantum yield in THF solution (1 mM), $\Phi_{F,P}$ = absolute quantum yield of the solid powders.

	$\lambda_{ab,DMSO}$ (nm)	$\lambda_{em,P}$ (nm)	$\lambda_{em,aggr}$ (nm)	$\lambda_{em,F}$ (nm)	$\Phi_{F,S}$ (%)	$\Phi_{F,P}$ (%)	ΔE (eV)	Dipole moments (Debye)
HBMA-1	284	545	535	541	0.22	8.46	3.80	2.79
HBMA-2	277	552	551	550	0.17	4.23	3.94	3.73
HBMA-3	305	574	567	566	0.35	3.58	3.37	2.27
HBMA-4	281	556	552	544	1.41	3.30	4.03	3.00

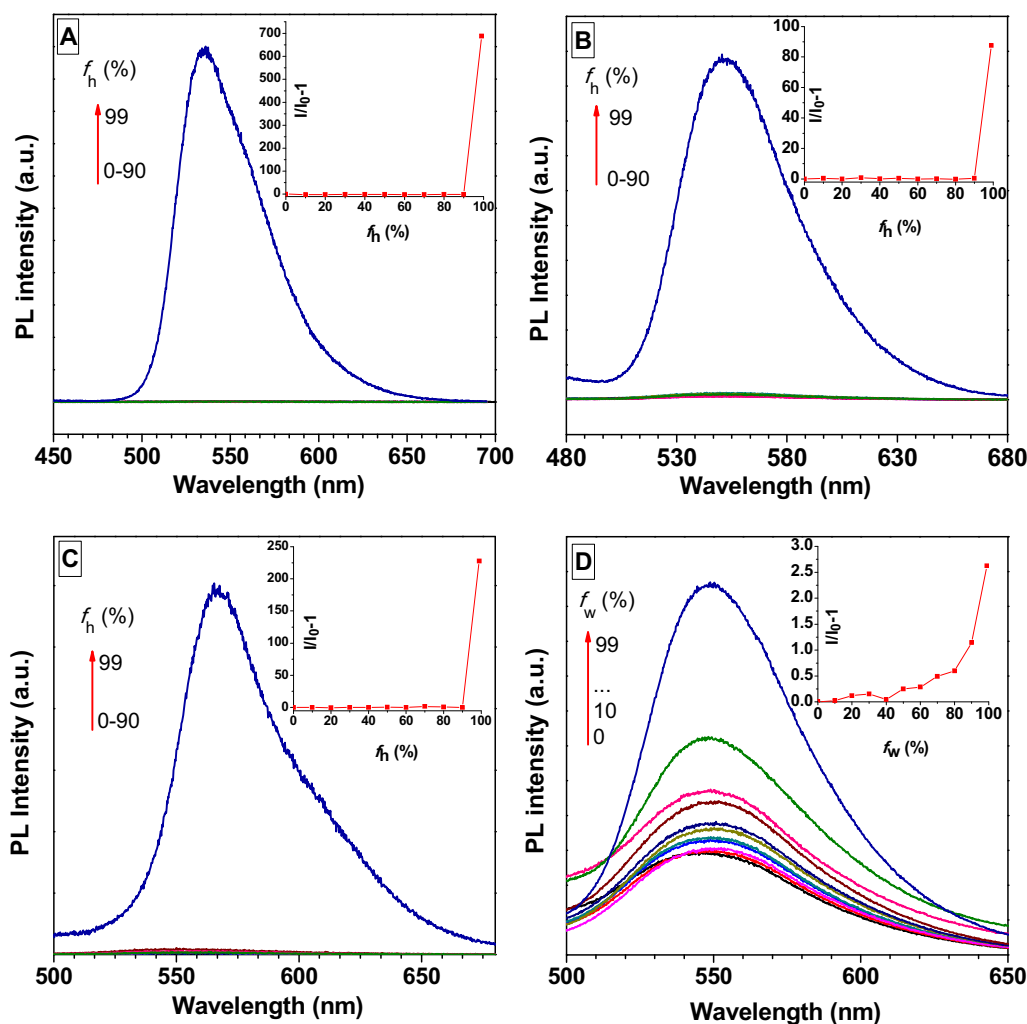


Fig. 2. PL spectra of HBMA-1 (A), -2 (B), and -3 (C) in THF/hexane mixtures. (D) PL spectra of HBMA-4 in DMSO/water mixture. Excitation wavelength: 350 nm (HBMA-1), 340 nm (HBMA-2), 375 nm (HBMA-3 and HBMA-4). Concentration: 1 mM. Plots of their relative PL intensity ($I/I_0 - 1$) at peak position versus f_h or f_w are shown in the insets of each figure.

indistinctive (2.6-fold) after forming aggregates at 99% water fraction (f_w). The above PL spectra indicate that the AIE performances depend highly on the position of D-A units. The excellent AIE property of HBMA-1 stems from the highly symmetrical para-position of its D-A units, which would favor the compact and well-ordered molecular packing. The free volume in the aggregation is thus shrunk to further suppress the intramolecular motion to enable higher emission efficiency. On the contrary, molecular asymmetry is easy to induce loose packing which allows limited rotational and/or vibrational motion and thus lowers the emission efficiency.

3.2. Intramolecular Charge Transfer

The sensitivity of HMBAs to solvent polarity was studied to probe their ICT effect. Take HBMA-1 for example, its absorption spectrum in hexane shows that the π - π^* absorption band peaks at around 276 nm (Fig. 3A). Moreover, it has a shoulder peak at 356 nm, which is ascribed to the CT transition. From non-polar solvents (i.e., hexane) to polar solvents (i.e., DMSO), a bathochromic-shift of π - π^* transition (276–284 nm), is recorded. Simultaneously, the CT band, which is relatively weak in hexane, EA and CHL, has increased remarkably in high-polar solvent such as DMF and DMSO. The π - π^* and CT absorption of the other compounds (including HBMA-2, 3 and 4) fall into the similar region as that of HBMA-1. In addition, their absorption spectra show a similar response toward solvent polarity: red-shift in π - π^* absorption band and enhancement in CT absorption band. It is worth mentioning

that the most remarkable bathochromic-shift was found with HBMA-3, which is as large as 30 nm. This result suggests the strongest ICT effect of HBMA-3, and agrees well with its longest emission wavelength of the solid-state spectra as seen in Fig. 1. The spectral changes including bathochromic shift and the gradually enhanced shoulder peak clearly demonstrate the formation of the CT state, especially in polar solvents. In the resulting CT state, solvent relaxation occurs with the intramolecular rotation of the D-A groups to a certain angle, resulting in a much weaker conjugation relative to its locally-excited state (plane conformation). Such twisted conformation will be stabilized by the polar solvent surrounded, giving rise to a much narrowed energy gap and the consequent red-shifts in the absorption bands [37,38].

DFT calculations on their energy levels were performed to prove the ICT process of the HMBAs. The HOMO and LUMO molecular orbital amplitude plots are shown in Fig. 4. Indeed from molecular simulation the distribution in the HOMO and LUMO electron clouds is asymmetrical for all the involved molecules. For instance, HOMO orbital of HBMA-1 is mainly located on the methyl benzene moiety and partially located on the other benzene ring, carboxylic group are excluded from electron delocalization due to its electron-deficiency. In contrast, the benzoic acid group has attracted a large proportion of LUMO electron, owing to its strong electronic withdrawing ability. The other compounds also exhibit asymmetrical electronic cloud distribution and their locations are similar to HBMA-1. In short, HOMO electron would be held due to the electronegativity of methyl benzene moiety, and it tends to shift to the benzoic acid in the LUMO orbital. Although the energy levels of both

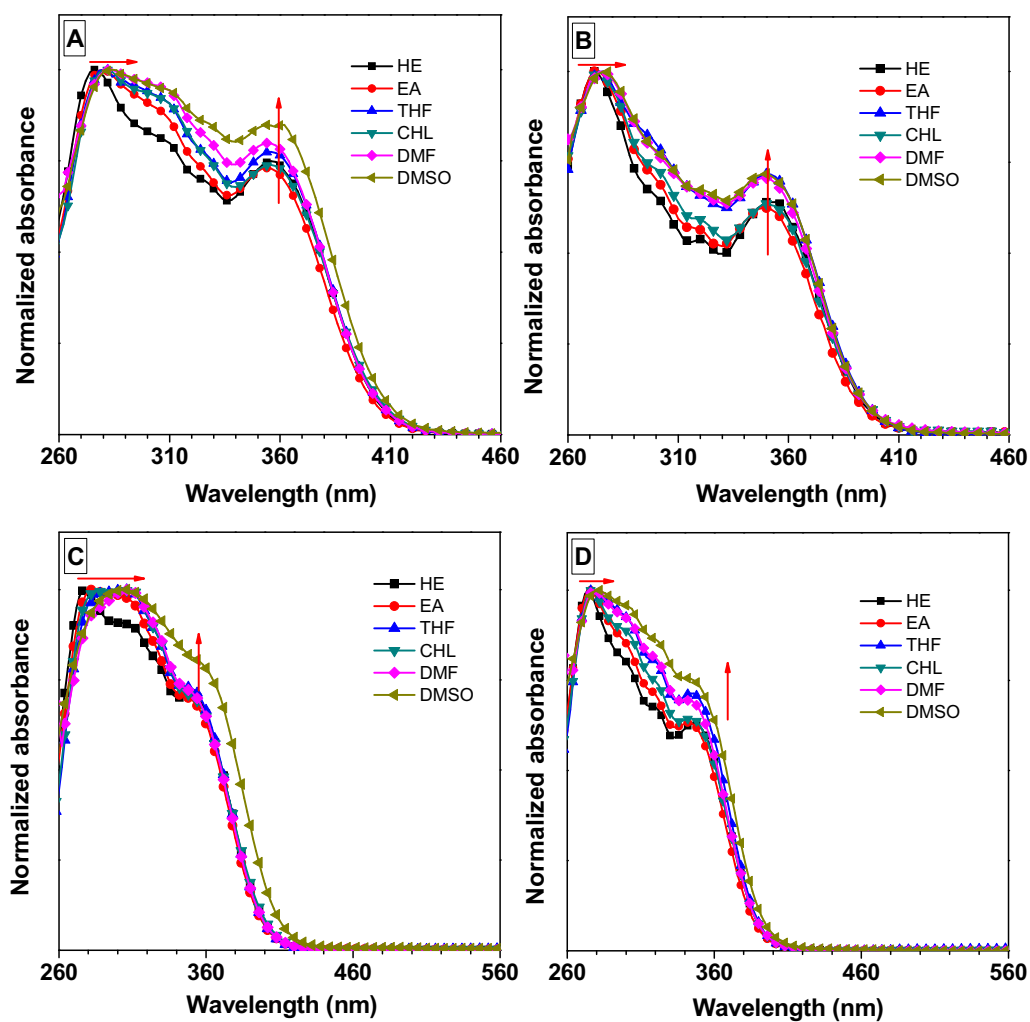


Fig. 3. Normalized UV-vis spectra of HBMA-1 (A), -2 (B), -3 (C) and -4 (D) in organic solvents with different polarities. Concentration: 10 μ M. Abbreviation: ethyl acetate (EA), tetrahydrofuran (THF), chloroform (CHL), *N,N*-dimethylformamide (DMF), dimethyl sulfoxide (DMSO).

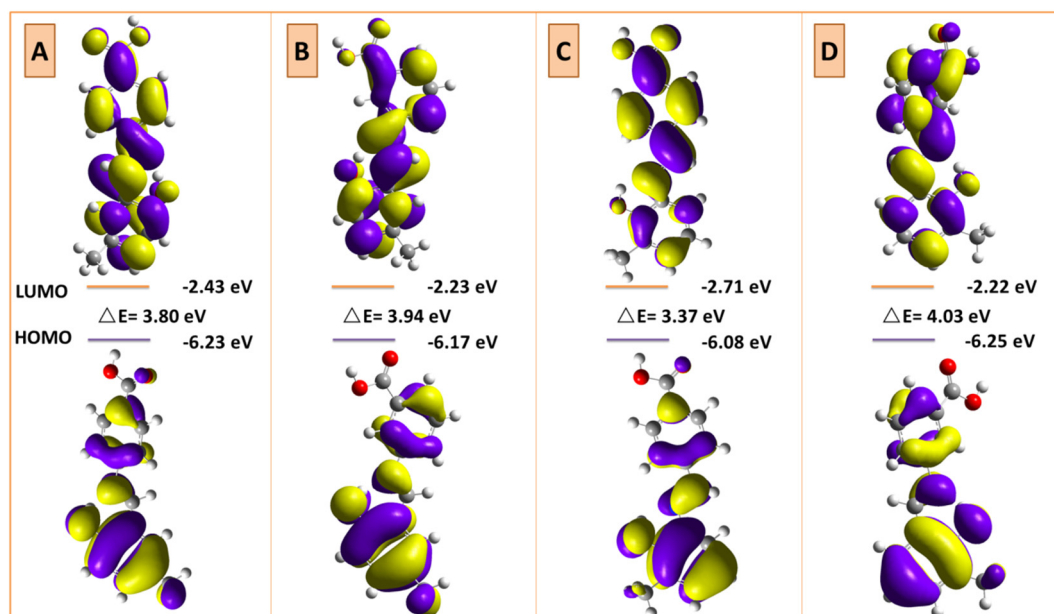


Fig. 4. Molecular orbital amplitude plots of the HOMO and LUMO energy levels of HBMA-1 (A), -2 (B), -3 (C) and -4 (D), calculated by using the B3LYP/6-31G* basis set.

HOMO and LUMO varies slightly with the position of D/A units, the result is consistent with that from spectral analysis and demonstrates that the lowest energy gap (3.37 eV) was obtained with HMBA-3 (Table 1), which has been proved to have the strongest ICT effects. It is clear that these solid emitters could change the emission color by simply varying the position of D/A groups to fine-tune the HOMO/LUMO energy levels.

3.3. Color-tuned and Shape-controlled Self-assembly

Molecular self-assembly is the process in which disordered molecules arrange themselves into an ordered system or even well-defined architectures as a consequence of specific intermolecular weak forces within the “building blocks”. These driving forces, including electrostatic interactions, hydrogen bonding, π - π stacking, dipole-dipole interaction, and hydrophilic/hydrophobic effect, have enabled diversiform supramolecular structures such as spheres, fibers, rods and helical structures [39–42]. Impressive as it is, many sensors would only function based on specific self-assembled structures [24,43]. For the HMBAs, D/A units not only adjust the direction of dipole moment but also serve as functional group, which would induce molecular self-assembly in totally different ways. In this section, we aim to illustrate the position effect of D/A units in self-assembly behavior.

The assembly of HMBA-1 was fabricated by drop-casting using chloroform solution (50 mM). It was then observed with a fluorescence microscopy as shown in Fig. 5A. It reveals that HMBA-1 has assembled into

two-dimensional square structure with kelly green fluorescence. SEM images in Fig. 5B and C reveal the fine structure of the squares, which are actually formed by closely stacked multilayer sheets with nanosized thickness and glaze surfaces. After natural evaporation of a few drops of chloroform solution (2 mM), HMBA-2 assembles into micro-sized rods with yellow fluorescence (Fig. 5D). As displayed in the SEM images (Fig. 5E and F), the diameter of the rod-like assemblies ranges from 0.5 to 2 μ m. It is difficult to estimate the aspect ratio because the micro rods are mostly interlaced. As expected, the longest emission wavelength (orange color) was obtained with HMBA-3 assemblies, which is formed by drop-casting its chloroform solution (2 mM) as well. As shown in Fig. 5G–I, HMBA-3 assembles into one-dimensional nanofilaments with diameter down to 100–500 nm and length up to hundreds of micrometers. Ordered assemblies are also formed by drop-casting technique (chloroform, 10 mM) using HMBA-4 molecules as the building blocks. The assemblies seem to be one-dimensional and emit yellow fluorescence upon excitation with a UV beam (Fig. 5J). We only got an obscure view of the HMBA-4 assemblies with fluorescence microscope due to the fact that they have fallen into nanoscale level. The ambiguity of the structural details was resolved by SEM, which exhibits that HMBA-4 forms flexible nanowires with their average width down to dozens of nanometers (Fig. 5K and L).

The above results indicate that a small change in D/A position would have large effects in the shape of self-assembly structures. If HMBA-1 is identified as the starting material, repositioning the carboxylic acid and methyl group could hence built the other three isomers. Quadrate

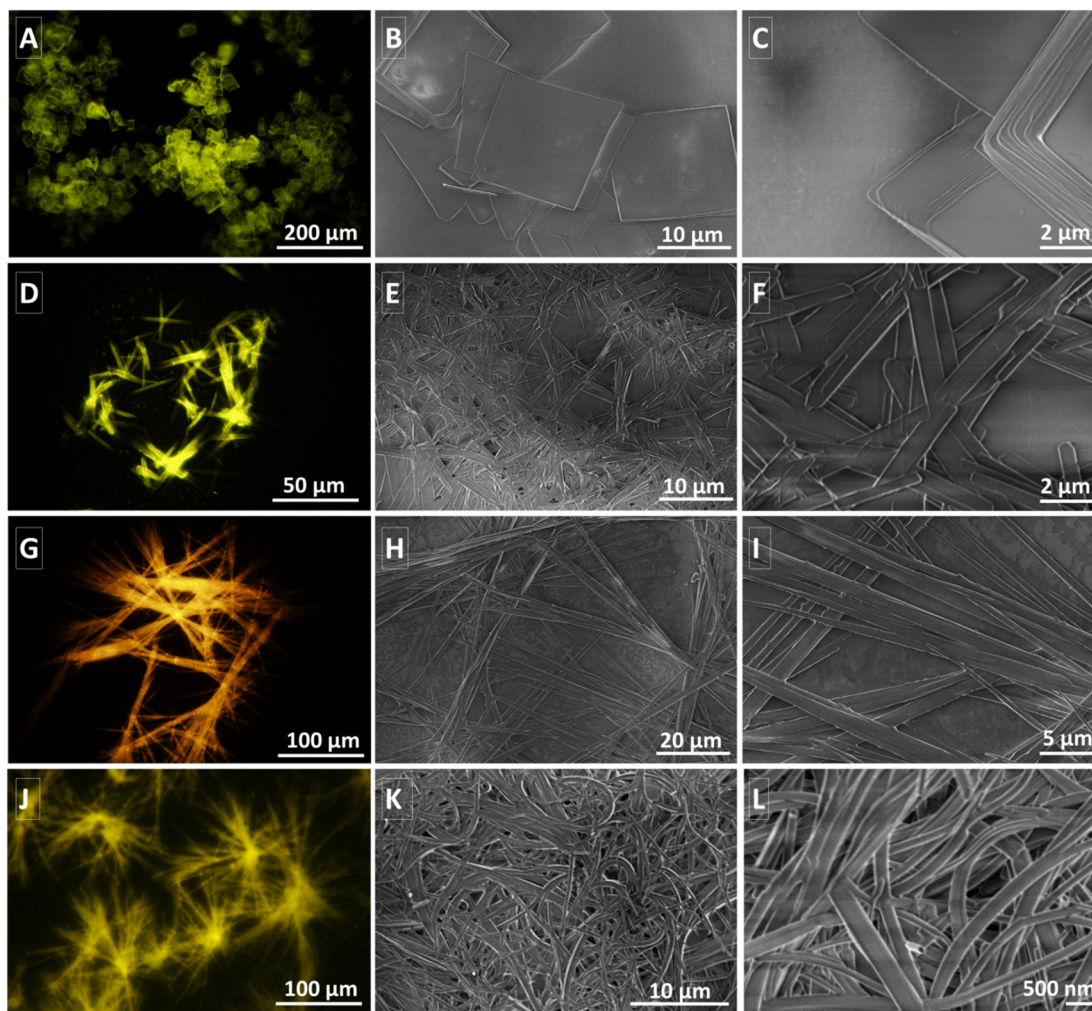


Fig. 5. Fluorescence microscopy images of self-assembly structures of HMBA-1 (A), -2 (D), -3 (G) and -4 (J) prepared by drop-casting using chloroform solution at room temperature. Excitation wavelength: 365 nm. SEM images showing the fine structure of HMBA-1 (B and C), -2 (E and F), -3 (H and I) and -4 (K and L).

sheets would turn into micro-rods when shifting carboxylic acid to meta-position. And changing the position of methyl groups would create nanofilaments. With carboxylic acid and methyl group both changed, flexible nanowires are obtained. Among the four compounds, the assembly of HMBA-4 shows the minimum scale, which endows it with the largest specific surface area. Therefore, its performances may be improved if it is fabricated into a sensor device. Besides, the diversified shapes of the molecular assemblies could be obtained through facile drop-casting process, in which no surfactants, patterned templates, or additives are needed. Such simplified technology makes the molecular system a reliable candidate for real application.

The shape-controllability of the self-assemblies stems from the inductive effect of D/A units. We anticipate that the direction of dipole-dipole interaction is the main driving force to organize molecules when self-assembling. When molecules start to aggregate from their solution, D unit (methyl group) would prefer to couple with A unit (carboxylic acid) rather than itself due to dipole-dipole interaction, as the former is electron-rich whereas the latter is electron-deficient. Such D-A coupling would correspond to a lowest energy state, compared with the other packing modes. Polarized by D-A units, the dipole moments of these molecules range from 2.27 Debye to 3.73 Debye as listed in Table 1. Molecules with meta-position substituents evidently show much higher dipole moment than those with para-position substituents due to molecular asymmetry. On the other hand, the molecules arranged in the assemblies also prefer to adopt the conformation with the minimal steric hindrance. Taking both sides into consideration, D/A units doubtlessly plays a vital role in governing the molecular self-assembly, as their location will directly influence the dipole-dipole interaction as well as the steric hindrance. As a result, D/A units in this molecular series can be visually regarded as “rotary knobs”: When the knobs rotate, i.e., D/A units relocate, the four states of the architecture will appear in sequence, including quadrature microsheets, microrods, nanofilaments and nanowires. In short, the rational molecular design of the HMBAs contributes to the nice controllability of their assembly structures, and further paves ways for developing novel smart materials with customized morphology to meet the needs of a given application.

3.4. Sensing Amine Gas

Benzoic acid moiety shows strong affinity to amines [44], and if its electron-withdrawing ability was disrupted by amines, the ICT process would be disturbed, offering the potential to cause fluorescent responses. A fluorescent sensor for amines can be created based on such mechanism. The necessity to innovate new amine sensors based on fluorescent signal is due to their high sensitivity, portability, fast response and easy visualization [45–47]. These advantages are exactly highly desired by food industry. In view of this, we fabricated a fluorescent sensor by depositing HMBA-1 assemblies on a quartz plate using the aforementioned methods, and then fixed it in the inner wall of a quartz cell. Ammonia water (14 M) was added to provide sufficient ammonia gas for fumigation. The PL spectrum of the sensor was collected once every 1 min for 25 min. As displayed in Fig. 6A, the emission intensity at 541 nm becomes progressively lower with an increase in the exposure time, and remains basically unchanged within a short time down to 10 min. HMBA-2 was also fabricated into a self-assembly film for the time-dependent measurement. In contrast, the spectrum peaked at 550 nm exhibits a slight decrease in the first minute and then shows slight growth (Fig. 6B). The rising tendency stops after 3 min, indicating a full interaction between ammonia gas and the sensor. The HMBA-3 self-assembly film was continuously fumed by ammonia under the same condition. Its time-dependent emission spectrum undergoes a remarkable decrease upon fumigation, suggesting a stronger interaction between the sensor and the analyte (Fig. 6C). As depicted in Fig. 6D, a much stronger emission induction relative to other three sensors was obtained with HMBA-4-loaded film in this time-dependent fumigation

experiment, suggesting the highest sensitivity. Additionally, an obvious hypochromatic shift from 545 nm to 534 nm was detected. The final quenching efficiencies of the four sensors are approximately 24.4, 4%, 49% and 96%, respectively. As listed in Table 1, the maximum emission wavelength of each molecule shows slight differences among three forms, i.e., solid powder, aggregates and film. This is owing to the ICT nature of the isomers, as the CT state is susceptible to multiple factors including chemical environment, steric hindrance and packing mode [37,38].

From the point of view of aggregation structures, such different spectral response can be partially ascribed to their characteristic morphologies with specific surface area differing from each other. HMBA-4 in possession of the largest specific surface area allows for stronger solid-gas interaction compared with the other three competitors. Furthermore, the self-assemblies of HMBA-4 is the most vulnerable to ammonia due to the nano-sized fine structure, it shows the most distinct visual change with continuous NH₃ fumigation under fluorescence microscope (Fig. 7A–D). In addition, the assemblies of HMBA-4 actually become obscured after fumigation as seen in Fig. 7D. This implies that the architecture of HMBA-4 is easy to be destructed upon fumigation. The disassembly of the HMBA-4 with the exposure of other organic amines including *n*-butylamine (Fig. S9A), diisopropylamine (Fig. S9B) and triethylamine (Fig. S9C) was also observed with fluorescence microscope. The reduced fluorescence together with the hypochromatic shift could be readily detected by naked eyes. The quenching efficiency is probably owing to the continuous collision between the HMBA-4 and ammonia, which would consume the energy of the excited molecule. And the hypochromatic shift may be ascribed to the changes in energy level of the molecule binding with ammonia. Besides, the disassembled structure (Fig. S10) together with the corresponding emission spectrum (Fig. S11) is unable to recover after thermal treatment, implying the single use of the sensing device.

The molecular stacking mode is also of great importance, as loose packing will help the analyte to enter the assembly structure while close packing is just the opposite. Stacked microsheet structure belongs to HMBA-1 is less sensitive as indicated in Figs. 6A and 7A, not only because it offers the smallest surface area for sensor-ammonia interaction, but also it is probably closely packed to inhibit the invasion of ammonia due to better molecular symmetry. Furthermore, relocating D/A units would vary the ICT process as discussed previously. If the A moiety (carboxylic acid) is attacked by amines, electron withdrawing ability would be changed to affect the spectrum, which may involve both intensity change and wavelength shifting. Besides, the emission of AIE compounds is sensitive to steric hindrance, therefore inserting ammonia molecule into the self-assembled architectures will further block the intramolecular motion to boost stronger emission. In conclusion, there are multiple factors that contribute to the spectral responses, including surface area, ICT effect and intermolecular volume, making the sensing performances vary with the type of the AIE isomers.

DFT calculations on electron cloud distribution and energy levels were performed in order to verify the mechanism of the spectral changes. As depicted in Fig. 8, the HOMO energy of HMBA-4-ammonia association is dominated by the orbital from the whole molecule except for carboxylic moiety. And there is no obvious change in the location of LUMO electron cloud, the energy level of both HOMO (−5.85 eV) and LUMO (−1.82 eV) was elevated when HMBA-4 was attacked by ammonia, suggesting a less stable state than that of the starting molecule (Fig. 4D). In that way, the electron deficiency of the carboxylic acid group would be remitted by the external ammonia molecule carrying lone pair electrons. This will weaken the electron withdrawing ability of the carboxylic acid group. As displayed in Fig. 8, we observed that electronic cloud exerts no shifting along the D-A direction when comparing HOMO to LUMO, implying that the strength and efficacy of the ICT process are reduced. The spectral changes including decrease in intensity and blue-shift in wavelength can be well explained by the calculation results.

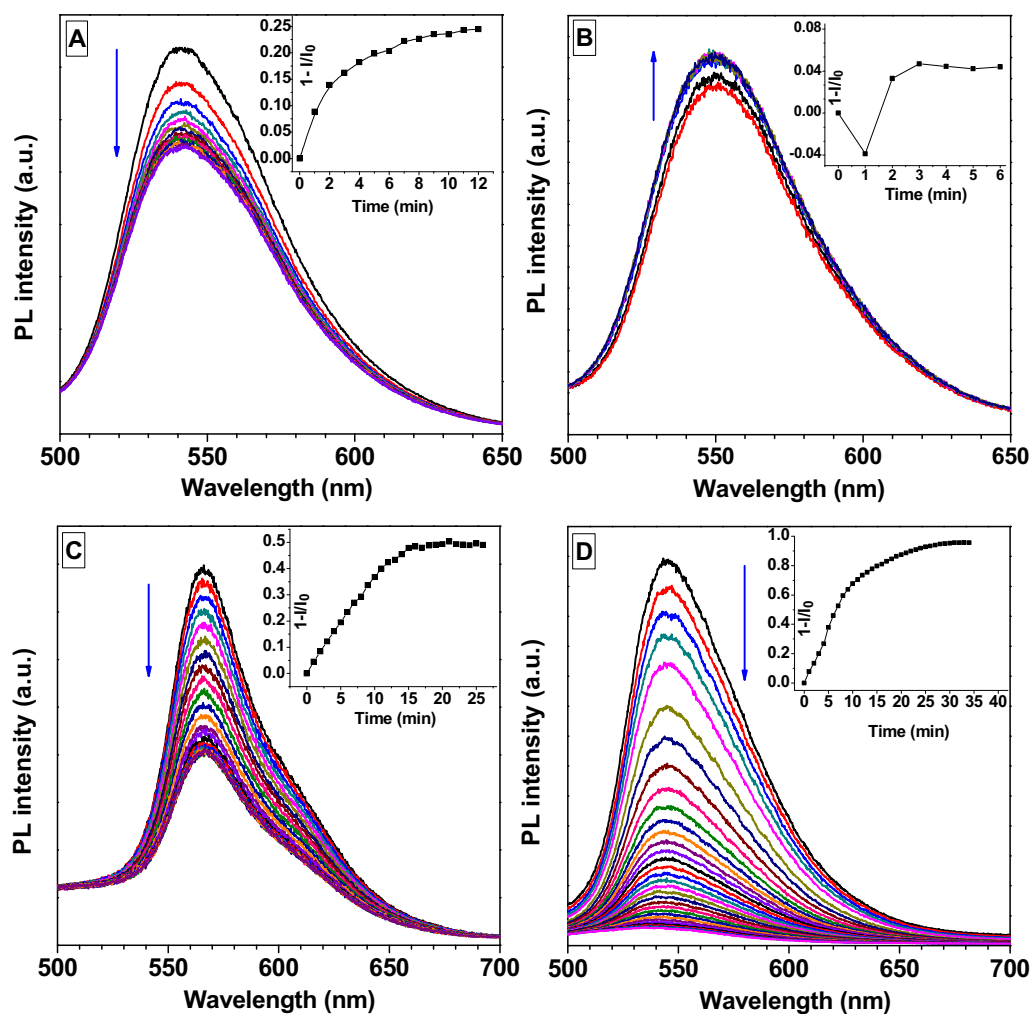


Fig. 6. Time-dependent PL spectra of the self-assembly film of HBMA-1 (A), -2 (B), -3 (C) and -4 (D) exposed to ammonia gas. Time interval: 1 min. Excitation wavelength: 350 nm (HMBA-1), 340 nm (HMBA-2), 375 nm (HMBA-3 and HMBA-4). Plots of their relative PL intensity $(I/I_0 - 1)$ at peak position versus time are shown in the insets of each figure.

The sensitivity analysis was estimated by a titration experiment, in which a self-assembly film of HMBA-4 was fixed in a quartz cell and then fumed by ammonia water with gradually increased concentrations. As shown in Fig. 9, the emission spectrum of self-assembly film undergoes a sustainable growth with the vapour pressure of ammonia ranging from 0 to 652 Pa, and then level off. The final-state emission has increased by 75% as plotted in the inset of Fig. 9. A linear equation is obtained via data fitting by using growth rate $(I/I_0 - 1)$ as a function of the square of vapour pressure. The detection limit (DL) of the sensor is determined to be 186 Pa according to the equation expressed as $DL = 3\sigma/k$ (σ stands for the standard deviation of the blank signal; k represents the slope of the linear equation). It is nice to see that signal of the sensor is enhanced rather than quenched, indicating that the ammonia gas adsorbed on the film is unable to disassemble the well-ordered structure of the sensor. Thus the AIE mechanism still dominates the emission process, in which the ammonia molecules have inserted into the self-assembly architecture to further block the intramolecular motion.

3.5. Sensing Meat Spoilage

Microorganisms could break down amino acids to yield various kinds of amines. In the meat spoilage process, amino acids can either degrade to ammonia through deamination, or to biogenic amines by decarboxylation, such as cadaverine, spermidine, putrescine and spermine [48]. Therefore, the abnormal high level of amines can be used to signal

the freshness of the meat products. Our aim is to test the response of the self-assembled film to amine vapours generated by meat samples. Fresh lean pork was purchased from a local supermarket and then cut into slices to make four samples for testing: Sample 1 is fresh pork, Sample 2, 3 and 4 were stored at room temperature for 24 h, 48 h and 72 h, respectively. All the samples were sealed in the quartz cell to produce amines before being measured. The HMBA-4 self-assembled films for meat monitoring were fabricated using the aforementioned method, with the average thickness of 4.6 μm . Then the films were continuously fumed by pork samples and their in-situ time-dependent spectra was recorded (Figs. S12–15). Fresh sample (Sample 1) exerts almost no change as seen in the tendency chart (Fig. 10). The fluorescence intensity varies by approximately 2%, which can be ascribed to instrumental error. In contrast, the pork sample stored for 24 h (Sample 2) causes intensity growth of 17% relative to the blank spectrum. This indicates that the amount of the amine gas generated by Sample 2 was too small to disassemble the film structure and thus the AIE mechanism of the probe would be strengthened to boost higher fluorescence. In sharp contrast, the emission intensity was reduced by 14% when the film was placed beside Sample 3, which has been stored for 48 h prior to use. Similarly, the film losses 40% of its starting intensity with the pork sample storing for 72 h (Sample 4). The quenching effect of the latter two samples implies the disassembly of the films and further indicates the spoilage of the pork, as a large amount of amine gas will be released. In addition, the spectra of the sensing films show an immediate change with putrid pork samples, and have completed the full spectral response

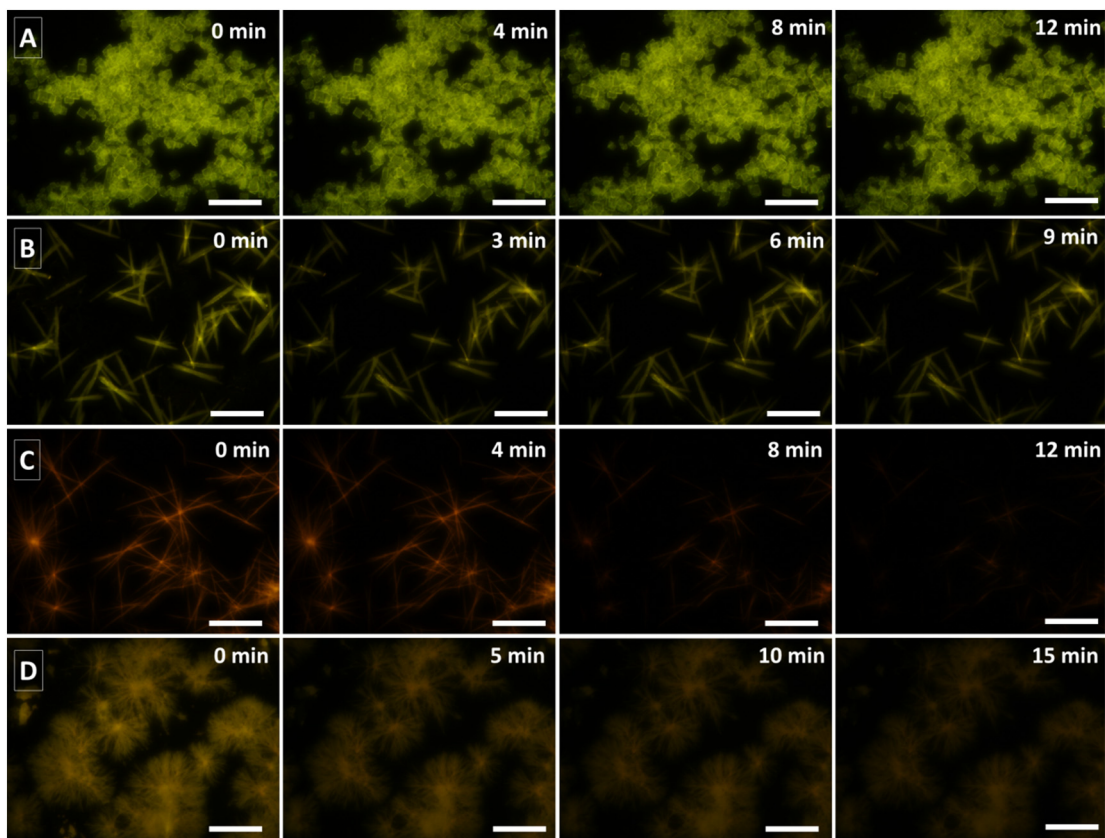


Fig. 7. Fluorescence microscopy images of the self-assembled film of HBMA-1 (A), -2 (B), -3 (C) and -4 (D) exposed to ammonia, taken at different time. Scale bar: 100 nm. Excitation wavelength: 365 nm.

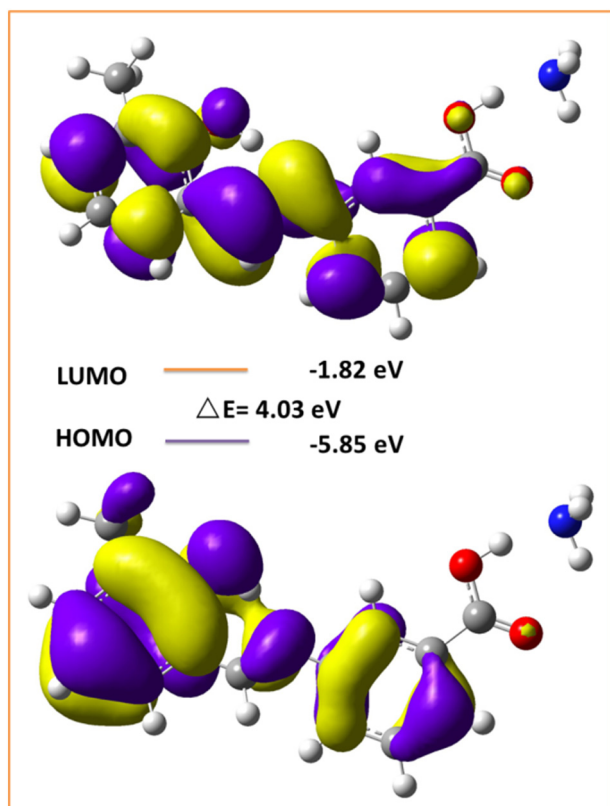


Fig. 8. Molecular orbital amplitude plots of the HOMO and LUMO energy levels of HBMA-4 combining with ammonia. Basis set: B3LYP/6-31G*.

within a short time down to 10 min. This suggests a fast detection which is highly desired in real-world application. This experiment demonstrates that HBMA-4 offers great potential to serve as a sensor for food spoilage monitoring, and its diversified signal responses would help to establish the standard for meat freshness.

4. Conclusion

The incorporation of D-A units to the synthesized positional isomers endows them with both AIE and ICT effect. Our systematic comparative

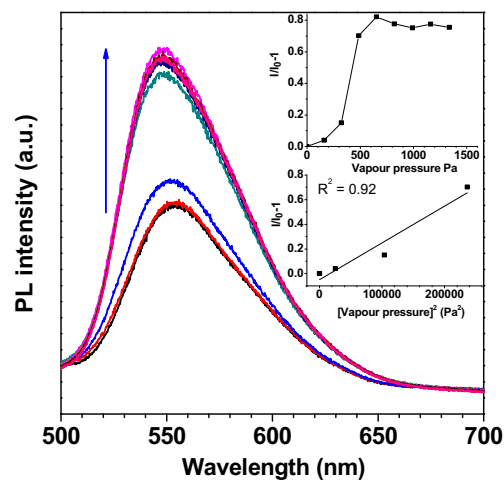


Fig. 9. PL spectra of HBMA-4 self-assembled film upon fumigation with ammonia water with different concentrations (0 mM, 0.1 mM, 0.2 mM...0.8 mM). Inset: relative change in maximum emission intensity versus [vapour pressure] and [vapour pressure]².

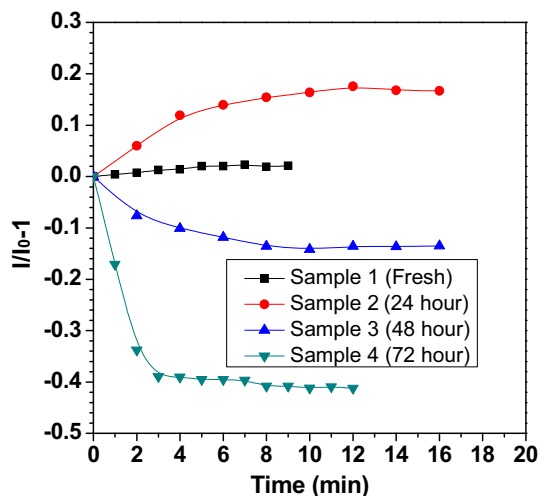


Fig. 10. Time-dependent fluorescence quenching profile of the HMBA-4 self-assembled film under the influence of pork samples. Time interval: 1 min. Excitation wavelength: 375 nm.

study leads to the discovery of their high controllability in the photophysical properties: their AIE properties, ICT effects and energy levels can be well controlled by the position of D-A units. Furthermore, HMBAs show the color-turned and shape-controlled self-assembly. The D/A units play a key role in guiding the molecular self-assembly, as their locations are closely related to the dipole-dipole interaction, which is exactly the main driving force for the self-assembly. With the D/A units repositioning, four types of the self-assembled architectures appear sequentially, including multilayer microsheets, microrods, nanofilaments and nanowires. The big difference in morphology suggests that a minor change in chemical structure would have significant impacts on the molecular self-assembly. In addition, amines would have impact of a different degree in the D-A efficacy of the HMBAs, which is reflected in the emission spectra as the response. Owing to the unique nanowire structure with largest specific area, HMBA-4 has the most distinct spectral response to amines compared with the other compounds. A reliable amine sensor is fabricated based on HMBA-4 assembly, which can serve as an indicator for meat. It succeeds in detecting the spoiled pork samples. This study may open a new area in nano/micromaterials science and facilitates the emergence of customized materials with the ability to modify their performances according to the needs.

Acknowledgments

Support is acknowledged from the National Natural Science Foundation of China (Grant Nos. 51703135, 21503139 and 11474204) and Project of Construction of Scientific Research Base under Beijing Municipal Education Commission (Grant Nos. KM201610028006 and KM201610028007). The corresponding author is also grateful for the support from Beijing Key Laboratory of Optical Materials and Photonic Devices.

Appendix A. Supplementary Data

Supplementary data to this article can be found online at <https://doi.org/10.1016/j.saa.2018.07.021>.

References

[1] P.J. Sarnoski, S.F. O'Keefe, M.L. Jahncke, P. Mallikarjunan, G.J. Flick, Analysis of crab meat volatiles as possible spoilage indicators for blue crab (*Callinectes sapidus*) meat by gas chromatography–mass spectrometry, *Food Chem.* 122 (2010) 930–935.
 [2] J.W. Marshall, P. Schmitt-Kopplin, N. Schuetz, F. Moritz, C. Roullier-Gall, J. Uhl, A. Colyer, L.L. Jones, M. Rychlik, A.J. Taylor, Monitoring chemical changes during food sterilisation using ultrahigh resolution mass spectrometry, *Food Chem.* 242 (2018) 316–322.

[3] F. Bibi, C. Guillaume, N. Gontard, B.G. Sorli, Wheat gluten, a bio-polymer to monitor carbon dioxide in food packaging: electric and dielectric characterization, *Sensors Actuators B Chem.* 250 (2017) 76–84.
 [4] K. Saetia, J.M. Schnorr, M.M. Mannarino, S.Y. Kim, G.C. Rutledge, T.M. Swager, P.T. Hammond, Spray-layer-by-layer carbon nanotube/electrospun fiber electrodes for flexible chemiresistive sensor applications, *Adv. Funct. Mater.* 24 (2014) 492–502.
 [5] R.R. Nair, N. Joshi, V.P. Boricha, S. Haldar, P.B. Chatterjee, Monitoring metabolite change in ice stored ghol fish (*Protonibea diacanthus*) by using a ^1H NMR technique: identification of pyruvate as a spoilage marker, *Anal. Methods* 8 (2016) 7030–7033.
 [6] N. Deepa, A.B. Ganesh, Design and development of portable opto-electronic sensing system for real-time monitoring of food fermentation, *Sensors Actuators B Chem.* 233 (2016) 674–683.
 [7] D.G. Santarossa, L.P. Fernandez, Development of on-line spectrofluorimetric methodology for selenium monitoring in foods and biological fluids using Chrome azurol S quenching, *Talanta* 172 (2017) 31–36.
 [8] S. Kim, S. Lee, Y. Ahn, H.K. Kim, J. Koh, S.D. Kim, B.G. Kim, A polydiacetylene-based colorimetric chemosensor for malondialdehyde detection: a food spoilage indicator, *J. Mater. Chem. C* 5 (2017) 8553–8558.
 [9] H. Wang, D.D. Chen, Y.H. Zhang, P. Liu, J.B. Shi, X. Feng, B. Tong, Y.P. Dong, A fluorescent probe with an aggregation-enhanced emission feature for real-time monitoring of low carbon dioxide levels, *J. Mater. Chem. C* 3 (2015) 7621–7626.
 [10] J. Shi, Y. Li, Q. Li, Z. Li, Enzyme-responsive bioprobes based on the mechanism of aggregation-induced emission, *ACS Appl. Mater. Interfaces* 10 (2018) 12278–12294.
 [11] Q. Li, Z. Li, The strong light-emission materials in the aggregated state: what happens from a single molecule to the collective group, *Adv. Sci.* 4 (2017) 1600484.
 [12] L.Y. Hu, J.Y. Sun, J.Q. Han, Y.A. Duan, T.Y. Han, An AIE luminogen as a multi-channel sensor for ethanol, *Sensors Actuators B Chem.* 239 (2017) 467–473.
 [13] Z. Arsov, I. Urbancic, J. Strancar, Aggregation-induced emission spectral shift as a measure of local concentration of a pH-activatable rhodamine-based smart probe, *190* (2018) 486–493.
 [14] Y.J. Cai, C. Gui, K. Samedov, H.F. Su, X.G. Gu, S.W. Li, W.W. Luo, H.H.Y. Sung, J.W.Y. Lam, R.T.K. Kwok, I.D. Williams, A.J. Qin, B.Z. Tang, An acidic pH independent piperazine–TPE AIEgen as a unique bioprobe for lysosome tracing, *Chem. Sci.* 8 (2017) 7593–7603.
 [15] Y.N. Hong, J.W.Y. Lam, B.Z. Tang, Aggregation-induced emission: phenomenon, mechanism and applications, *Chem. Commun.* (2009) 4332–4353.
 [16] Z.K. Zhang, R. Tian, W.J. Zhou, Y.J. Lin, C. Lu, Aggregation-induced emission assembled ultrathin films for white light-emitting diodes, *Chem. Commun.* 53 (2017) 12676–12679.
 [17] J. Mei, N.L.C. Leung, R.T.K. Kwok, J.W.Y. Lam, B.Z. Tang, Aggregation-induced emission: together we shine, united we soar! *Chem. Rev.* 115 (2015) 11718–11940.
 [18] Y.N. Hong, J.W.Y. Lam, B.Z. Tang, Aggregation-induced emission, *Chem. Soc. Rev.* 40 (2011) 5361–5388.
 [19] M. Gao, S.W. Li, Y.H. Lin, Y. Geng, X. Ling, L.C. Wang, A.J. Qin, B. Tang, Fluorescent light-up detection of amine vapors based on aggregation-induced emission, *ACS Sens.* 1 (2016) 179–184.
 [20] Z.G. Chi, X.Q. Zhang, B.J. Xu, X. Zhou, C.P. Ma, Y. Zhang, S.W. Liu, J.R. Xu, Recent advances in organic mechanofluorochromic materials, *Chem. Soc. Rev.* 41 (2012) 3878–3896.
 [21] C. Vijayakumar, G. Tobin, W. Schmitt, M.J. Kim, M. Takeuchi, Detection of explosive vapors with a charge transfer molecule: self-assembly assisted morphology tuning and enhancement in sensing efficiency, *Chem. Commun.* 46 (2010) 874–876.
 [22] L. Wang, R. Yang, J.J. Li, L.B. Qu, P.D. Harrington, High-sensitive electrochromic sensor of Sudan I based on template-directed self-assembly of graphene–ZnSe quantum dots hybrid structure, *Sensors Actuators B Chem.* 215 (2015) 181–187.
 [23] X.H. Cao, Q.Q. Ding, N. Zhao, A.P. Gao, Q.S. Jing, Supramolecular self-assembly system based on naphthalimide boric acid ester derivative for detection of organic amine, *Sensors Actuators B Chem.* 256 (2018) 711–720.
 [24] T.Y. Han, W. Wei, J. Yuan, Y. Duan, Y.P. Li, L.Y. Hu, Y.P. Dong, Solvent-assisted self-assembly of an AIE + TICT fluorescent Schiff base for the improved ammonia detection, *Talanta* 150 (2016) 104–112.
 [25] J. Chen, Y. Wang, W.Y. Li, H.P. Zhou, Y.X. Li, C. Yu, Nucleic acid-induced tetraphenylethene probe noncovalent self-assembly and the superquenching of aggregation-induced emission, *Anal. Chem.* 86 (2014) 9866–9872.
 [26] J. Han, Y. Li, J. Yuan, Z. Li, R. Zhao, T. Han, T. Han, To direct the self-assembly of AIEgens by three-gear switch: morphology study, amine sensing and assessment of meat spoilage, *Sensors Actuators B Chem.* 258 (2018) 373–380.
 [27] W.Z. Yuan, Y. Gong, S. Chen, X.Y. Shen, J.W.Y. Lam, P. Lu, Y. Lu, Z. Wang, R. Hu, N. Xie, H.S. Kwok, Y. Zhang, J.Z. Sun, B.Z. Tang, Efficient solid emitters with aggregation-induced emission and intramolecular charge transfer characteristics: molecular design, synthesis, photophysical behaviors, and OLED application, *Chem. Mater.* 24 (2012) 1518–1528.
 [28] J.Q. Han, Z.F. Li, P.J. Shi, F. Li, Y.A. Duan, T.Y. Han, A chemosensor for fingerprinting liquors: implication for differentiation and identification, *Sensors Actuators B Chem.* 248 (2017) 101–107.
 [29] M.H. Chua, H. Zhou, T.T. Lin, J.S. Wu, J.W. Xu, Triphenylethylene-based donor-acceptor-donor molecules: studies on structural and optical properties and AIE properties for cyanide detection, *J. Mater. Chem. C* 5 (2017) 12194–12203.
 [30] J.Y. Sun, J.Q. Han, Y. Liu, Y.A. Duan, T.Y. Han, J. Yuan, Mechanochromic luminogen with aggregation-induced emission: implications for ink-free rewritable paper with high fatigue resistance and low toxicity, *J. Mater. Chem. C* 4 (2016) 8276–8283.
 [31] L.L. Bu, J.Q. Chen, X.D. Wei, X. Li, H. Agren, Y.S. Xie, An AIE and ICT based NIR fluorescent probe for cysteine and homocysteine, *Dyes Pigments* 136 (2017) 724–731.
 [32] V.S. Padalkar, D. Sakamaki, K. Kuwada, N. Tohrai, T. Akutagawa, K. Sakai, S. Seki, AIE active triphenylamine-benzothiazole based motifs: ESIPT or ICT emission, *RSC Adv.* 6 (2016) 26941–26949.

- [33] C. Niu, L. Zhao, T. Fang, X. Deng, H. Ma, J. Zhang, N. Na, J. Han, J. Ouyang, Color- and morphology-controlled self-assembly of new electron-donor-substituted aggregation-induced emission compounds, *Langmuir* 30 (2014) 2351–2359.
- [34] E. Ravindran, E. Varathan, V. Subramanian, N. Somanathan, Self-assembly of a white-light emitting polymer with aggregation induced emission enhancement using simplified derivatives of tetraphenylethylen, *J. Mater. Chem. C* 4 (2016) 8027–8040.
- [35] L.L. Zhang, K.C. Liang, L.C. Dong, P.P. Yang, Y.Y. Li, X. Feng, J.G. Zhi, J.B. Shi, B. Tong, Y.P. Dong, Aggregation-induced emission enhancement and aggregation-induced circular dichroism of chiral pentaphenylpyrrole derivatives and their helical self-assembly, *New J. Chem.* 41 (2017) 8877–8884.
- [36] J. Pitchaimani, A. Kundu, S. Karthikeyan, S.P. Anthony, D. Moon, V. Madhu, A crab claw shaped molecular receptor for selective recognition of picric acid: supramolecular self-assembly mediated aggregation induced emission and color change, *CrystEngComm* 19 (2017) 3557–3561.
- [37] Z.R. Grabowski, K. Rotkiewicz, W. Rettig, Structural changes accompanying intramolecular electron transfer: focus on twisted intramolecular charge-transfer states and structures, *Chem. Rev.* 103 (2003) 3899–4031.
- [38] S. Sasaki, G.P.C. Drummen, G. Konishi, Recent advances in twisted intramolecular charge transfer (TICT) fluorescence and related phenomena in materials chemistry, *J. Mater. Chem. C* 4 (4) (2016) 2731–2743.
- [39] P. Singh, L.S. Mittal, V. Vanita, K. Kumar, A. Walia, G. Bhargava, S. Kumar, Self-assembled vesicle and rod-like aggregates of functionalized perylene diimide: reaction-based near-IR intracellular fluorescent probe for selective detection of palladium, *J. Mater. Chem. B* 4 (2016) 3750–3759.
- [40] S.D. Bhagat, A. Srivastava, Rods, helices and spherulites: diverse selfassembled architectures from L-phenylalanine derivatives, *CrystEngComm* 18 (2016) 4369–4373.
- [41] R.V. Bell, C.C. Parkins, R.A. Young, C.M. Preuss, M.M. Stevens, Assembly of emulsion droplets into fibers by microfluidic wet spinning, *J. Mater. Chem. A* 4 (2016) 813–818.
- [42] H. Liu, X.B. Shen, Z.G. Wang, A. Kuzyk, B.Q. Ding, Helical nanostructures based on DNA self-assembly, *Nano* 6 (2014) 9331–9338.
- [43] Y.J. Li, T.F. Liu, H.B. Liu, M.Z. Tian, Y.L. Li, Self-assembly of intramolecular charge-transfer compounds into functional molecular systems, *Acc. Chem. Res.* 47 (2014) 1186–1198.
- [44] T.Y. Han, J.W.Y. Lam, N. Zhao, M. Gao, Z.Y. Yang, E.G. Zhao, Y.P. Dong, B.Z. Tang, A fluorescence-switchable luminogen in the solid state: a sensitive and selective sensor for the fast “turn-on” detection of primary amine gas, *Chem. Commun.* 49 (2013) 4848–4850.
- [45] T.Y. Han, X. Feng, B. Tong, J.B. Shi, L. Chen, J.G. Zhi, Y.P. Dong, A novel “turn-on” fluorescent chemosensor for the selective detection of Al^{3+} based on aggregation-induced emission, *Chem. Commun.* 48 (2012) 416–418.
- [46] Y. Li, Y. Deng, X. Zhou, J. Hu, A label-free turn-on-off fluorescent sensor for the sensitive detection of cysteine via blocking the Ag^+ -enhancing glutathione-capped gold nanoclusters, *Talanta* 179 (2018) 742–752.
- [47] Z.F. Gao, A.Y. Ogbe, E.E. Sann, X. Wang, F. Xia, Turn-on fluorescent sensor for the detection of glucose using manganese dioxide–phenol formaldehyde resin nanocomposite, *Talanta* 180 (2018) 12–17.
- [48] P. Alam, N.L.C. Leung, H.F. Su, Z.J. Qiu, R.T.K. Kwok, J.W.Y. Lam, B.Z. Tang, A highly sensitive bimodal detection of amine vapours based on aggregation induced emission of 1,2-dihydroquinoxaline derivatives, *Chem. Eur. J.* 23 (2017) 14911–14917.